

Engineering photomagnetism in collinear van der Waals antiferromagnets

M. Na*,¹ V. Radovskaia*,^{1, a)} D. Khusyainov,² P. Kim,² K. Mukhuti,^{2, 3} P. C. M. Christianen,^{2, 3} E. Kochetkova,⁴ A. Isaeva,^{4, 5, 6} A. de Visser,⁴ D. Pashov,⁷ M. V. Schilfgaarde,⁸ E. H. T. Teo,^{9, 10} A. Chaturvedi,¹¹ S. Acharya,⁸ Th. Rasing,² A. V. Kimel,² and D. Afanasiev^{2, b)}

¹⁾*Radboud University, Institute for Molecules and Materials, 6525 AJ Nijmegen, The Netherlands*

²⁾*Radboud University, Institute for Molecules and Materials, 6525 AJ Nijmegen, The Netherlands*

³⁾*HFML-FELIX, Toernooiveld 7, 6525 ED Nijmegen, the Netherlands*

⁴⁾*Institute of Physics, University of Amsterdam, Science Park 904, Amsterdam 1098 XH, The Netherlands*

⁵⁾*Department of Physics, Technische Universität Dortmund, 44227 Dortmund, Germany*

⁶⁾*Research Center Future Energy Materials and Systems, 44227 Dortmund, Germany*

⁷⁾*King's College London, Theory and Simulation of Condensed Matter, The Strand, WC2R 2LS London, UK*

⁸⁾*Materials, Chemical and Computational Science Directorate, National Laboratory of the Rockies, Golden, CO, 80401 USA*

⁹⁾*School of Electrical and Electronic Engineering, Nanyang Technological University, Singapore 639798, Singapore*

¹⁰⁾*School of Materials Science and Engineering, Nanyang Technological University, Singapore 639798, Singapore*

¹¹⁾*Temasek Laboratories, Nanyang Technological University, 50 Nanyang Drive, 637553, Singapore*

Achieving efficient ultrafast optical control of antiferromagnetic spin dynamics is a central goal for next-generation high-speed THz spintronic and magnonic devices. Resonant optical pumping of crystal-field-split $d-d$ orbital multiplets in magnetic TM ions directly modulates exchange and spin-orbit interactions, inducing large-amplitude coherent spin precession. However, such effects are limited to a handful of systems and there is no general strategy to enhance $d-d$ photomagnetism in antiferromagnets. Here, we demonstrate the engineering of photomagnetism via TM-ion doping in collinear van der Waals antiferromagnets. In $\text{Mn}_{1-x}\text{Ni}_x\text{PS}_3$, small amounts of Ni^{2+} activate a strong photomagnetic response while largely preserving the Néel ground state. Even 10% Ni boosts the response by more than an order of magnitude compared to pure MnPS_3 , with resonant pumping of Ni^{2+} $d-d$ transitions driving large-amplitude coherent spin precession and providing helicity-dependent phase control. Tuning the pump energy across the full $\text{Mn}_{1-x}\text{Ni}_x\text{PS}_3$ composition range shows that Ni excitations remain effective across competing Néel and zig-zag antiferromagnetic states while supporting tunable-frequency coherent spin precession. These results establish TM-ion doping as a versatile strategy to harness orbital multiplet excitations for ultrafast, low-dissipation spin control in van der Waals antiferromagnets.

*These authors contributed equally.

^{a)}Electronic mail: viktorii.radovskaia@ru.nl

^{b)}Electronic mail: d.afanasiev@science.ru.nl

I. INTRODUCTION

Photomagnetism, the direct control of magnetic states through resonant light-matter interactions¹ offers a route toward ultrafast and energy-efficient spin manipulation beyond the limits of magnetic-field-based approaches^{2–4}. To date, photomagnetism has been observed across a wide range of material platforms, from single-molecule magnets^{5,6}, to ferro- and antiferromagnetically (AFM) ordered solids^{7–9}. Unlike optomagnetic effects, such as the inverse Faraday¹⁰ or Cotton-Mouton effects¹¹, which are non-dissipative and, in principle, do not require photon absorption, photomagnetic effects rely explicitly on absorption and are therefore expected to be highly efficient in controlling spins¹². Photon absorption promotes specific electronic or phononic excitations that modify orbital occupations and, consequently, magnetic anisotropy and exchange interactions^{9,13–17}. Such resonant control provides a fundamentally different paradigm from laser-induced heating, opening tantalizing prospects for coherent manipulation of spins.

This capability is particularly critical in collinear antiferromagnets. Their vanishing net magnetization precludes conventional magnetic-field control, while their intrinsic terahertz spin dynamics demand optical-bandwidth excitation with spin-precession amplitudes sufficient for switching^{4,18–20}. Among available strategies, the resonant optical pumping of crystal-field split orbital multiplets, such as localized $d-d$ and $f-f$ transitions in transition-metal ($3d$) and rare-earth ($4f$) antiferromagnets, has emerged as a promising route^{7,8,14,21,22}. In magnetic transition-metal (TM) ions, these transitions are nominally parity- (Laporte) and spin-forbidden in centrosymmetric environments and acquire oscillator strength only through symmetry breaking mechanisms^{23,24}, for example via vibronic coupling, local lattice distortions, or hybridization with ligands. Nevertheless, recent progress has shown that resonant femtosecond pumping of these states can generate exceptionally strong photomagnetic responses, despite low absorption. In particular, resonant $d-d$ photoexcitation can drive large-amplitude spin precession in AFMs by transiently modifying exchange interactions¹⁵, anisotropy^{8,14,25,26}, and has even enabled switching between metastable states in ferrimagnets^{7,22}. Yet, a predictive framework for engineering a coherent photomagnetic response in collinear antiferromagnets remains lacking. Understanding why certain orbital transitions drive giant coherent spin motion whereas others – even within the same magnetic ion – remain ineffective is therefore a central and unresolved challenge^{14,15,27–29}.

In this work, we aim to elucidate the fundamental principles governing the efficacy of $d-d$ orbital multiplet excitations by engineering the coherent response in alloys of NiPS₃ and MnPS₃. These isostructural compounds belong to the TM-thiophosphate family of van der Waals antiferromagnets^{30,31}, renowned for their exceptionally strong light-matter interactions, pronounced excitonic correlations, and, most importantly, their ability to launch large-amplitude coherent spin dynamics through resonant pumping of $d-d$ orbital transitions^{8,14,26,28,32–34}. These two TM ions host different orbital manifolds, spin multiplicities, and spin-orbit couplings, which lead to different antiferromagnetic ground states^{31,35–37}. By partially substituting Mn with Ni in the Mn_{1– x} Ni _{x} PS₃ series, we get an opportunity to tune the magnetic ground state between the Néel order of MnPS₃ and the zig-zag order of NiPS₃. This substitution also enables a direct comparison of the photomagnetic responses of Mn²⁺ and Ni²⁺ ions, achieved by scanning the pump photon energy across their respective $d-d$ multiplet resonances and measuring the amplitude of the resulting collective spin dynamics. Strikingly, at 10% Ni – where the Néel ground state of MnPS₃ is preserved – the spin precession driven by Ni²⁺ multiplets is nearly 15× larger than that generated by Mn²⁺ multiplets, while also providing helicity-dependent phase control, absent in pure MnPS₃. Moreover, it is the ³A_{1g} multiplet excitation – a minor feature in the absorption spectrum of NiPS₃ – that emerges as the most efficient driver of spin dynamics, surpassing all Mn²⁺ multiplets and the more optically absorptive Ni²⁺ multiplets.

Supported by quasiparticle self-consistent $G\hat{W}$ (QSG \hat{W}) theory^{38–40} – which allows direct visualization of the excited-state orbital wavefunctions – we identify the key factors that govern the photomagnetic response of different multiplet excitations: (i) although Mn²⁺ transitions involve spin-flip and directly couple to spins, their weak oscillator strength makes them far less effective than the optically stronger, spin-conserving Ni²⁺ resonances; (ii) the strongest drivers of spin precession are those excitations with highly localized wavefunctions that lie away from the fundamental bandgap and minimize hybridization with the surrounding sulfur ligand field; and (iii) the lowest-energy Ni²⁺ ³A_{1g} state carries substantial orbital angular momentum, and couples more efficiently to the spin degree of freedom than other Ni²⁺ multiplet excitations. Optical pumping of this resonance, therefore, generates coherent spin-precessions with amplitudes more than an order of magnitude larger than those observed via Mn²⁺ excitations. Altogether, our findings establish the orbital degree of freedom as a powerful driver of spin dynamics and demonstrate that strategic ion substitution offers a versatile route for shaping the photomagnetic response and controlling collective excitations in collinear antiferromagnets.

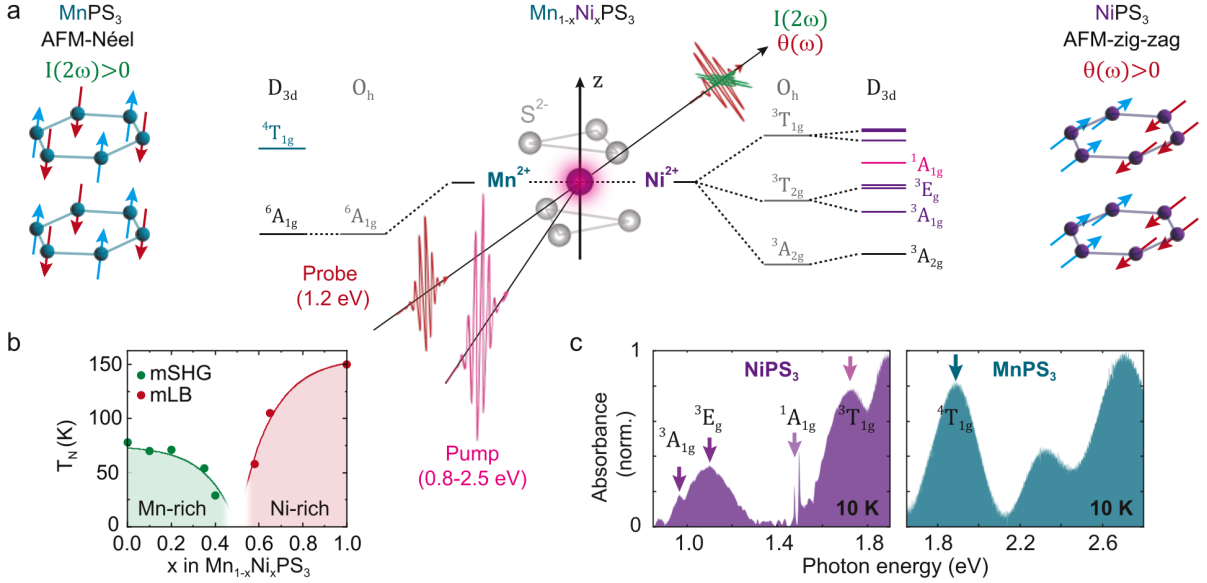


Figure 1. Tuning the antiferromagnetic ground state and photomagnetic properties of $\text{Mn}_{1-x}\text{Ni}_x\text{PS}_3$. (a) The transition-metal (TM) ions form a hexagonal lattice and are surrounded by trigonally-distorted S_6 octahedral cages. The Tanabe-Sugano diagram of Mn^{2+} and Ni^{2+} ions in the octahedral (O_h) crystal field with a trigonal (D_{3d}) distortion is shown in the center, along with spin-flip excited states. MnPS_3 (left) favours a Néel (N)-type antiferromagnetic (AFM) order with the Néel vector out-of-plane. In contrast, the larger spin-orbit coupling leads to an in-plane anisotropy for NiPS_3 and zig-zag (ZZ) AFM order (right). In the pump-probe experiment, the laser fundamental (1.2 eV) is detuned from the multiplet resonances and is used as a probe. The pump pulse, with an incident fluence of 6 mJ/cm^2 , is tuned from 0.8 to 2.4 eV across multiple multiplet resonances. (b) The ground state magnetic phase diagram of $\text{Mn}_{1-x}\text{Ni}_x\text{PS}_3$ mapped by symmetry-selective magneto-optical probes. The spatial inversion symmetry breaking in the N-type AFM order gives magnetic second-harmonic generation (mSHG, green) and the ZZ-type order gives magnetic linear birefringence (mLB, red); these probes are used to determine the onset of the AFM order at the Néel temperature (T_N). The Mn (Ni)-rich compounds have an N (ZZ)-type AFM ground state reflective of the pure compound, while long-range magnetic order is not observed for $x = 0.5$. (c) Optical absorbance of pure NiPS_3 and MnPS_3 compounds measured at 10 K, showing the below-bandgap multiplet resonances.

II. TUNING MAGNETISM IN THE MIXED-COMPOUNDS

The $\text{Mn}_{1-x}\text{Ni}_x\text{PS}_3$ samples were grown via chemical vapor transport⁴¹ and characterized with energy-dispersive X-ray spectroscopy (EDS) to confirm a homogeneous elemental distribution (see Supplementary Sec. 1). In their pure forms, MnPS_3 and NiPS_3 both adopt a monoclinic crystal structure that can be described as a hexagonal lattice of TM- S_6 distorted octahedra with a phosphorus dimer in the center. Despite their structural similarities, the magnetic properties of MnPS_3 and NiPS_3 differ due to the distinct orbital occupation of the TM ions and the resulting spin configuration^{31,42,43}. MnPS_3 adopts a Néel (N)-type order while NiPS_3 exhibits a zigzag (ZZ)-type order, as shown in the left and right schematics of Fig. 1a. The N-type AFM ground state breaks spatial inversion symmetry, resulting in a significant second-order susceptibility and the emergence of magnetic second-harmonic generation (mSHG) below $T_N = 78 \text{ K}$ ⁴⁴. The ZZ-type AFM ground state in NiPS_3 preserves spatial inversion symmetry; however, the formation of extended ferromagnetic chains induces strong optical anisotropy, which manifests as magnetic linear birefringence (mLB) below $T_N = 155 \text{ K}$ ^{45–47}. Furthermore, the Néel vector is out-of-plane in MnPS_3 , which is known for the weakest single-ion anisotropy in the family⁴⁸. In contrast, in NiPS_3 a significantly larger single-ion anisotropy aligns the Néel vector in-plane^{49,50}.

To characterize the AFM ground state of the mixed $\text{Mn}_{1-x}\text{Ni}_x\text{PS}_3$ compounds we employ the two symmetry-selective magneto-optical probes mSHG and mLB. In Fig. 1b, we combine the temperature-dependence of mSHG (green) and mLB (red) to generate an AFM ground state phase diagram for $\text{Mn}_{1-x}\text{Ni}_x\text{PS}_3$, as a function of temperature and the Ni fraction x . The experimental methods and examples of the mSHG and mLB temperature dependencies are shown in Supplementary Sec. 2. We observe that only Mn-rich samples ($x < 0.5$) exhibit mSHG, while mLB only occurs in Ni-rich samples ($x > 0.5$). This trend suggests that the quantitatively dominant TM ion dictates the type of AFM order, with Mn-rich compositions favouring the N-type and Ni-rich compositions favouring the ZZ-type ground state. Further, we observe a suppression of T_N upon mixing. The suppression reflects the competition

between AFM nearest-neighbour exchange preferred by Mn ions and the FM nearest-neighbour exchange preferred by Ni ions, which destabilizes long-range magnetic order and leads to the disappearance of both the mLB and mSHG signals at half-mixing ($x = 0.5$). This observation is in line with previous studies indicating that compositions near $x = 0.5$ may host a spin-glass ground state⁵¹.

III. OPTICALLY-INDUCED COLLECTIVE SPIN DYNAMICS

Having established the AFM ground state, we turn to the photomagnetically-induced coherent spin dynamics. In the ground state of both MnPS_3 (${}^6A_{1g}$) and NiPS_3 (${}^3A_{2g}$), the orbital angular momentum is largely quenched by the octahedral crystal field. Even so, resonant excitation to higher-energy orbital multiplets – ${}^3T_{2g}$ (≈ 1 eV), ${}^1A_{1g}$ (≈ 1.5 eV) in Ni^{2+} and ${}^4T_{1g}$ (≈ 1.9 eV) in Mn^{2+} – has been shown to drive collective spin precession in their respective pure compounds^{14,26,28,52}. These resonances, shown schematically in Fig. 1a appear as distinct absorption peaks in the below-bandgap optical absorption spectra (Fig. 1c) and can be accessed by tuning the pump photon energy $h\nu$. Importantly, the Mn and Ni multiplet excitations are well separated in energy and do not spectrally overlap, allowing for a direct and unambiguous comparison of their efficiency in driving coherent magnons.

We begin with the Mn-rich sample $\text{Mn}_{0.65}\text{Ni}_{0.35}\text{PS}_3$ ($x = 0.35$) where the Mn to Ni ratio is approximately 2:1. This ensures substantial contribution from both magnetic ions while preserving a robust N-type ground state. The incident pump fluence is fixed at 6 mJ/cm^2 , and the pump photon energy is tuned from 0.8 to 2.5 eV to span the full range of Mn and Ni multiplet resonances. Spin dynamics are monitored using transient changes in the magnetic second-harmonic generation (ΔmSHG) in a transmission geometry, with a linearly polarized probe at 1.2 eV – outside the multiplet resonance range of either ion. The pump-induced dynamics as a function of pump-probe delay is shown in Fig. 2a. Here we present only the coherent oscillatory component of the data; for the raw data and the analysis procedure, see Supplementary Sec. 3. The data show that the oscillation amplitude depends strongly on the pump photon energy, with the largest response observed at 0.94 eV (purple).

The Fourier transform of the oscillations (Fig. 2b) reveals two modes with frequencies of 45 and 25 GHz. Their magnetic origin is evident from their temperature dependence (see Supplementary Sec. 4). As the temperature increases, a pronounced softening of the largest-amplitude 45 GHz mode towards $T_N = 52 \text{ K}$ is observed – characteristic of an antiferromagnetic magnon. To highlight the resonances that most effectively drive spin dynamics, we plot the Fourier spectra of the oscillations as a function of pump photon energy $h\nu$. Here, we extract the intensity of the 45 GHz mode by integrating the intensity between the two white lines in Fig. 2b. The spectral weight as a function of $h\nu$ shown at the top of Fig. 2b is best fit with four Gaussian curves, which peak at $E_{\text{pk}} = [0.925(10), 0.98(4), 1.498(10), 1.71(5)] \text{ eV}$, closely matching the ${}^3A_{1g}$, 3E_g , ${}^1A_{1g}$ and ${}^3T_{1g}$ optical absorption peaks of Ni^{2+} ions (see Fig. 1c). The two lowest-energy peaks – ${}^3A_{1g}$, 3E_g – derive from the doubly-degenerate ${}^3T_{2g}$ orbital multiplet in an ideal O_h crystal field and are split here by the trigonal distortion of the S_6 octahedra. Remarkably, despite Mn being the dominant magnetic species in the mixture, no indication of photoinduced spin precession is observed when the pump photon energy $h\nu$ is tuned into resonance with the $\text{Mn}^{2+} {}^6A_{1g}$ to ${}^4T_{1g}$ transition at 1.9 eV. This absence is particularly striking because the Mn^{2+} orbital excitation intrinsically involves a spin-flip process ($\Delta S = 1$), and its optical excitation is therefore expected to couple directly to the spin sector, potentially launching a large-amplitude coherent spin-wave response. The lack of such a response indicates that in the considered mixture, the Ni^{2+} crystal-field excitations provide the dominant pathway for driving coherent antiferromagnetic spin dynamics.

To highlight the exceptional spin response to the Ni^{2+} multiplet excitations, we performed the same measurements on $\text{Mn}_{0.9}\text{Ni}_{0.1}\text{PS}_3$ ($x = 0.1$), see Fig. 2c. This composition is strongly Mn-rich with a 9:1 Mn:Ni ratio, nearly five times higher than in $\text{Mn}_{0.65}\text{Ni}_{0.35}\text{PS}_3$, and has a robust N-type antiferromagnetic ground state (see Fig. 1b). Similarly to $\text{Mn}_{0.65}\text{Ni}_{0.35}\text{PS}_3$, the pump-photon-energy dependent Fourier spectrum in Fig. 2 also reveals two modes with frequency 92 GHz and 39 GHz. The higher-frequency mode is softened relative to the doubly degenerate zone-center magnon in pure MnPS_3 at 120 GHz⁵³, indicating a reduction of the effective exchange interactions induced by Ni substitution. The appearance of the lower-frequency mode points to a lifting of the magnon degeneracy, which we attribute to the progressive development of in-plane anisotropy promoted by Ni^{2+} ions⁴³. As described above, increasing the Ni fraction to $x = 0.35$ results in a further renormalization of the two modes to 45 and 25 GHz, consistent with the progressive modification of exchange interactions and anisotropy.

Figure 2d reveals that although the enhanced Mn fraction makes the contribution of the spin-flip $\text{Mn}^{2+} {}^4T_{1g}$ multiplet resonance to the excitation of spin precession discernible, its overall impact on the magnetic system remains weak. In contrast, photoexcitation of the minority Ni^{2+} multiplets results in the unambiguous excitation of coherent spin dynamics. Even more unexpectedly, despite having the

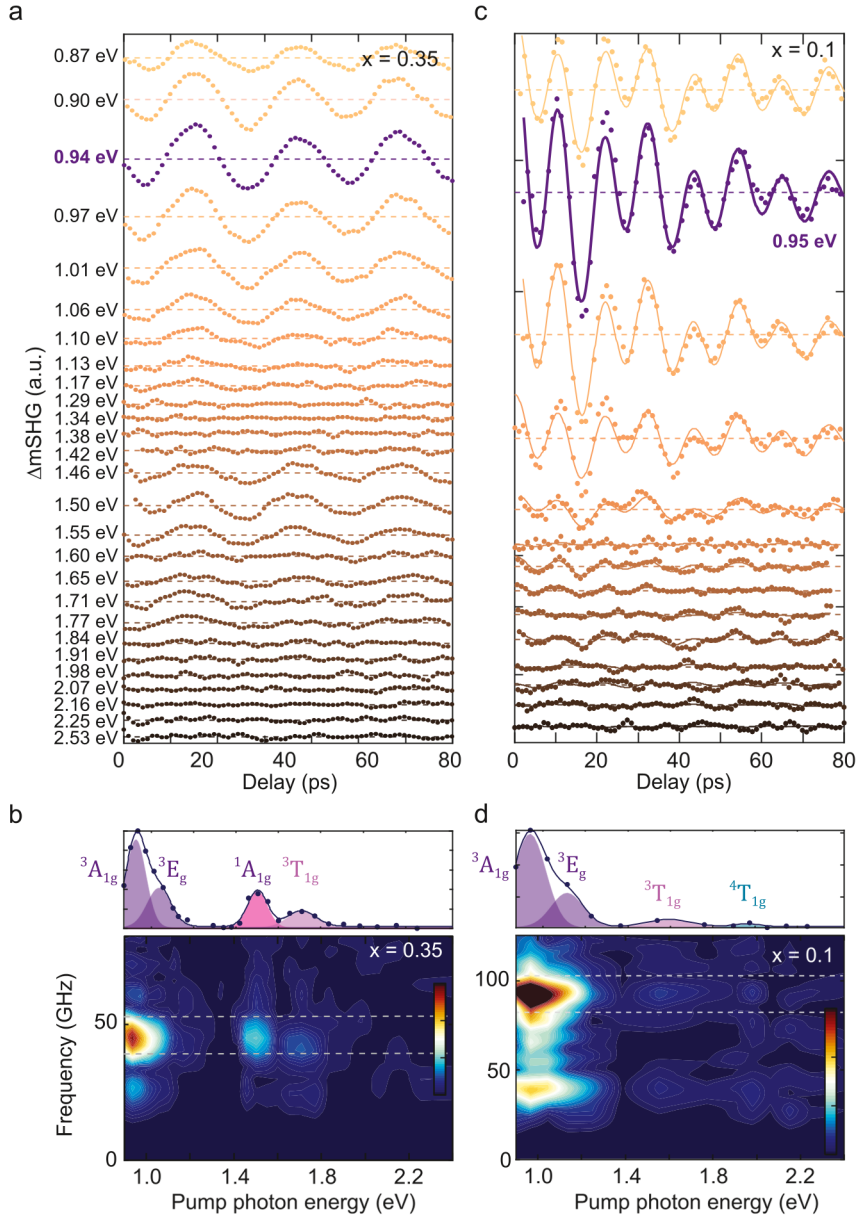


Figure 2. Launching coherent spin dynamics via resonant multiplet excitation in $\text{Mn}_{1-x}\text{Ni}_x\text{PS}_3$. (a, c) The pump-induced change of the magnetic second harmonic signal (ΔmSHG) as a function of pump-probe delay measured for $x = 0.35$ and $x = 0.1$ at $T = 10$ K, respectively. The trace at 0.94 (0.95) eV is highlighted. (b, d) The frequency spectrum of the coherent dynamics as a function of pump photon energy in the $x = 0.35$ and $x = 0.1$ samples. Colors indicate ΔmSHG intensity in linear scale. In panel b, clear resonances are observed at $E_{\text{Ni}} = [0.925, 0.97, 1.498, 1.708]$ eV, corresponding to multiplet resonances in Ni^{2+} in the trigonally distorted octahedra. In panel d, a clear resonance is observed at 0.95 eV, and smaller resonances at 1.55, and 1.98 eV, corresponding to multiplet excitations in Ni^{2+} (purple) and Mn^{2+} (turquoise). The intensity between the gray dashed lines is integrated and shown for the $x = 0.35$ (left) and $x = 0.1$ (right) samples and fit with four Gaussian peaks.

smallest absorption cross section, the ${}^3A_{1g}$ resonance drives the largest amplitude magnons, even in the $x = 0.1$. In contrast, the ${}^1A_{1g}$ and ${}^3T_{1g}$ resonances are only tentatively identified for the $x = 0.1$ sample, reflecting the reduced Ni concentration. Altogether, these observations show that the spin oscillations are photomagnetically driven by the selective excitation of specific multiplet resonances. The absence of any scaling with optical absorption rules out a heat-driven mechanism and identifies the dynamics as fundamentally nonthermal.

The large photomagnetic response of $\text{Mn}_{1-x}\text{Ni}_x\text{PS}_3$ to the weakly-absorbing ${}^3A_{1g}$ and 3E_g resonances could in principle be attributed to the increased pump penetration depth, as the transmitted second-

harmonic signal is most sensitive to the back surface of the sample. To ensure the observed photomagnetism is not due to a difference in pump fluence at the back surface, we complemented the ΔmSHG measurements in transmission for the $x = 0.1$ sample with ΔmSHG in reflection and ΔmLB in transmission – probes that are significantly less sensitive to pump-probe penetration depth mismatch. These complementary probes – shown in the Supplementary Sec. 5 – consistently reveal that the $\text{Ni}^{2+} {}^3A_{1g}$ resonance drives magnons with higher amplitude than other multiplet excitations.

To account for the pronounced sensitivity of the collective spin precession to specific Mn^{2+} and Ni^{2+} orbital transitions, it is essential to consider both how photoexcited orbital states couple to the spin system and how efficiently light drives the corresponding $d-d$ transitions. We begin by comparing the orbital excitations of Mn^{2+} and Ni^{2+} ions, which exhibit radically different photomagnetic responses. All Mn^{2+} excitations from the high-spin ${}^6A_{1g}$ ground state are spin-flip in character ($\Delta S = 1$), whereas most Ni^{2+} transitions are spin conserving ($\Delta S = 0$). Although spin-flip processes might be expected to couple more directly to magnetic order, the experiments show the opposite: even at a Mn:Ni ratio of 9:1, the Mn ${}^4T_{1g}$ resonance drives magnons with amplitudes nearly 15 times smaller than those generated by the weak Ni ${}^3A_{1g}$ transition. The stark contrast therefore cannot be explained by the spin character of the transitions alone, but instead reflects how efficiently the optical field couples to the respective orbital excitations. The weak photomagnetic response of Mn is rather consistent with the suppression of oscillator strength in $d-d$ transitions that involve a spin flip and are known to reduce optical coupling by up to two orders of magnitude^{40,54}. Consequently, despite providing a formally direct magnetic pathway, pumping of the Mn excitations is far less effective than that of the optically stronger, spin-conserving Ni resonances, which dominate the observed coherent photomagnetic response.

However, oscillator strength alone cannot account for the large photomagnetic response of the ${}^3A_{1g}$ excitation, which is a relatively weak absorption feature among Ni multiplet resonances. To highlight the relative efficiency of the photomagnetic orbital-to-spin coupling, we took the maximum amplitude of the driven spin precession in the $\text{Mn}_{0.7}\text{Ni}_{0.3}\text{PS}_3$ sample (from Fig. 2b) and normalized it by the corresponding maximum of the absorption spectrum, obtaining a value of orbital-to-spin coupling strength χ_{so} . Plotting these values as a histogram (see Fig. 3a) reveals a clear trend, showing that the ${}^3A_{1g}$ orbital state couples significantly more strongly to the spins compared with the 3E_g and ${}^3T_{1g}$ states, despite its weaker optical absorption.

To understand the origin of these differences, we analyze the excited states using the *ab-initio* many-body perturbation theory (MBPT) framework, $\text{QSG}\hat{W}$ ³⁸, which provides a detailed description of the electronic structure of $\text{Mn}_{1-x}\text{Ni}_x\text{PS}_3$ (details in Supplementary Sec. 6). Using this approach, we calculated the single-particle electronic structure for $x = 0.25$ compositions, approximating the experimental samples, modeled in a 40-atom supercell; see Extended Data Fig. 1. While the top of the valence bands shows strong hybridization between Mn- d and S- p states, the conduction bands are predominantly of Ni- d character. The occupied Ni- d states are located near -0.75 eV, as detailed in reference⁵⁴, which provides a comprehensive analysis of the one- and two-particle properties of Ni and Mn compounds individually. Importantly, the multiplet excitations observed in the material are excitonic in nature rather than single-particle transitions.

Using these results, we first analyze the real-space excitonic wavefunctions of the closely spaced ${}^3A_{1g}$ and 3E_g states. Although both originate from the ${}^3T_{2g}$ level, split by the trigonal distortion of the S_6 octahedra in NiPS_3 ^{55,56}, they exhibit very different photomagnetic orbital-to-spin coupling strength χ_{so} . Figure 3b-c show that the hole wavefunctions of both states are localized on the Ni ion, with ${}^3A_{1g}$ lying primarily in the xy -plane and 3E_g extending along the z -axis. The projection of the single-particle valence wavefunctions onto the excitonic hole component, shown in Extended Data Fig. 1, demonstrates that both states have e_g character, corresponding to orbital angular momenta $m_l = |2|$ and 0, largely associated with the $d_{x^2-y^2}$ and d_{z^2} orbitals, respectively. The ${}^3A_{1g}$ multiplet is more heavily weighted toward $m_l = |2|$, resulting in stronger spin-orbit coupling, whereas 3E_g has smaller orbital angular momentum and weaker coupling. Consequently, the ${}^3A_{1g}$ excitation couples more effectively to the spin sector, consistent with the larger magnon amplitude it drives.

We finally analyze the ${}^3T_{1g}$ excitation, which, despite having the strongest absorption, exhibits minimal orbital-to-spin coupling strength χ_{so} . Unlike the highly localized ${}^3A_{1g}$ and 3E_g states, ${}^3T_{1g}$ lies near the Ni band edge at 1.7 eV, indicating weaker excitonic binding and a delocalized wavefunction^{54,57}. As shown in Fig. 3d, the ${}^3T_{1g}$ hole-wavefunction extends across several hexagon plaquettes. Momentum-space decomposition (Extended Data Fig. 1h) reveals that the excitonic wavefunction is dominated by S- p valence states, which do not produce a change in the Ni orbital angular momentum and therefore couples only weakly to the spin sector. Consequently, the ${}^3T_{1g}$ resonance is inefficient in driving coherent spin dynamics, consistent with previous reports on orbital pumping in NiPS_3 , where this excitation produced no appreciable magnon response¹⁴.

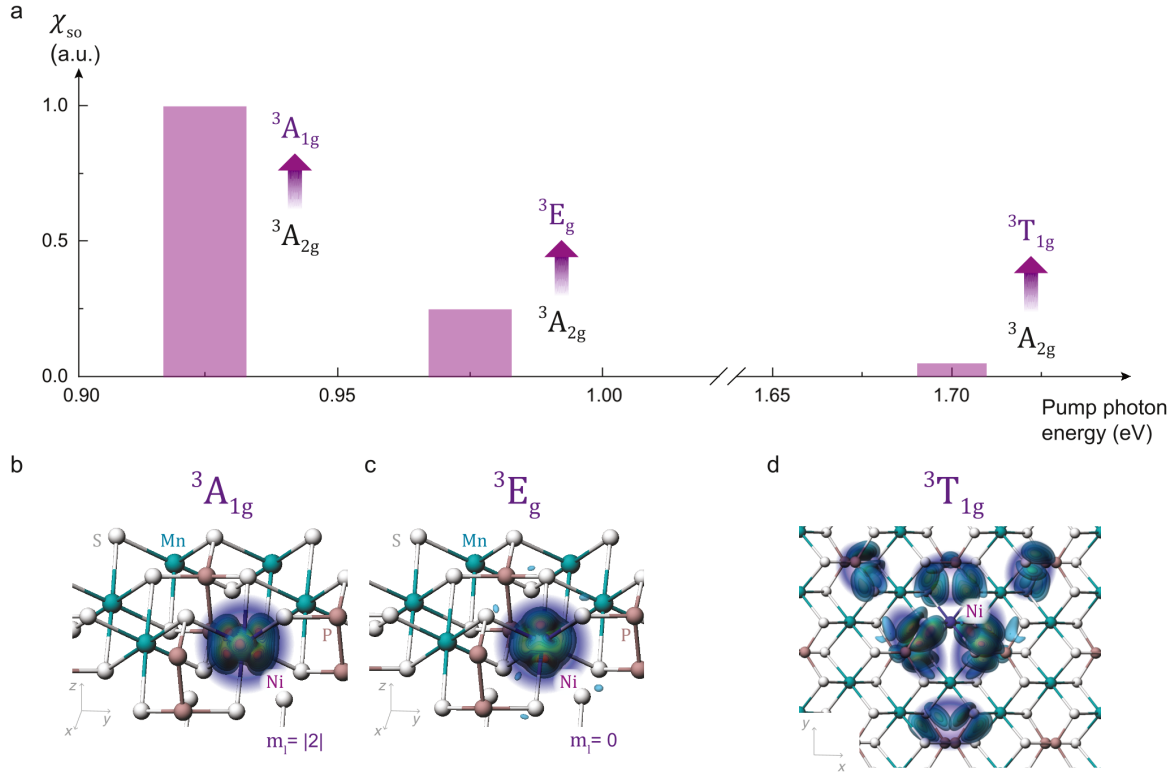


Figure 3. Spin-orbit efficiency of Ni^{2+} excitations in $\text{Mn}_{0.75}\text{Ni}_{0.25}\text{PS}_3$. (a) The orbital-to-spin coupling strength χ_{so} of the ${}^3A_{1g}$, 3E_g and ${}^3T_{1g}$ multiplets, which is calculated as the intensity of the spin dynamics (the amplitude of the corresponding Gaussian peaks in Fig. 2b) divided by the absorption peaks (the values of absorption at corresponding photon energies in NiPS_3 presented in Fig. 1c) and normalized to 1. (b-d) The wavefunction of the excitonic-hole for the (b) ${}^3A_{1g}$, (c) 3E_g and (d) ${}^3T_{1g}$ multiplets. The Ni and Mn ions are shown in purple and turquoise, respectively. S and P are shown in gray and brown. The ${}^3A_{1g}$ and 3E_g excitations are localized to the Ni-ion, while the ${}^3T_{1g}$ state is delocalized over multiple hexagonal plaquette. $m_l = |2|, (0)$ labels the Ni d states onto which the ${}^3A_{1g}$ (3E_g) excitation is projected.

IV. PHASE CONTROL OF MAGNONS IN $\text{Mn}_{1-x}\text{Ni}_x\text{PS}_3$

Having identified the Ni ${}^3A_{1g}$ excitation as the most efficient trigger of spin dynamics, even at low concentrations, we now examine how it can also be used to control these dynamics. In NiPS_3 , the amplitude and phase of spin precession driven by the ${}^3A_{1g}$ multiplet can be controlled by both the helicity of a circularly-polarized pump and the orientation of a linearly-polarized pump³⁴. In contrast, MnPS_3 shows no reported polarization-dependent control. To test whether the ${}^3A_{1g}$ multiplet excitation can impart similar control of spin waves in $\text{Mn}_{1-x}\text{Ni}_x\text{PS}_3$, we study the linear polarization and helicity dependence of the magnon phase as a function of the Ni fraction ($0.1 \leq x \leq 0.9$). Spin dynamics are tracked through the pump-induced change in magneto-linear birefringence (ΔmLB), which provides a composition-independent readout even in samples where the equilibrium mLB is absent.

Fig. 4a shows the spin dynamics induced by circularly-polarized pump pulses for the $x = 0.1$ and $x = 0.35$ samples. We observe no helicity-dependent response in the $x = 0.1$ sample; however, with increasing Ni content, a π phase shift emerges between opposite helicities – consistent with reports on pure NiPS_3 ^{14,34}. A similar trend is observed in the linear polarization dependence (Fig. 4b): The $x = 0.1$ sample shows no phase and amplitude variation, whereas both appear at $x = 0.2$. More data are presented in Supplementary Sec. 7. This onset coincides with a change in the magnetic anisotropy seen in magnetometry (see Supplementary Sec. 8), in which the Néel vector orientation becomes fully in-plane. Figure 4c summarizes the magnon frequencies and helicity dependence across the $\text{Mn}_{1-x}\text{Ni}_x\text{PS}_3$ series, with black (pink) circles corresponding to the absence (presence) of helicity dependence. Except for $x = 0.1$, the ${}^3A_{1g}$ resonance enables both efficient magnon generation and optical control over magnon amplitude and phase – even in Mn-rich compositions where the antiferromagnetic ground state is N-type.

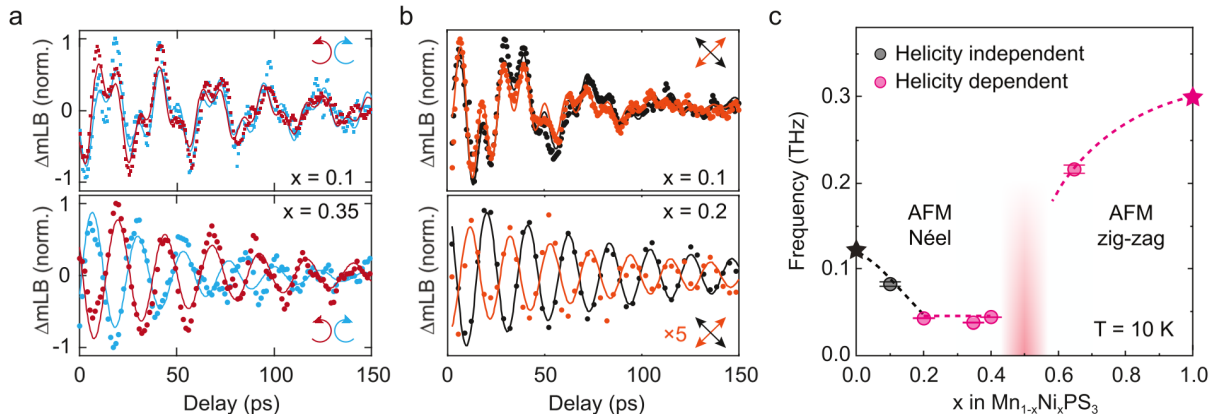


Figure 4. Phase control of spin dynamics in $\text{Mn}_{1-x}\text{Ni}_x\text{PS}_3$. (a) Helicity dependence of the magnon excitation for the $x = 0.1$ (top) and $x = 0.35$ (bottom) samples at 10 K. (b) Linear polarization dependence of the magnon excitation for the $x = 0.1$, $x = 0.2$ samples, respectively, at 10 K. The orange curve in the bottom panel is vertically scaled by a factor of 5 for visualization purposes. (c) Frequency of the magnons driven by the $\text{Ni } ^3A_{1g}$ excitation (0.95 eV) as a function of Ni fraction, measured with magnetic linear birefringence. Black (magenta) colors indicate the absence (presence) of phase-flip. The star markers for $x = 0$ and $x = 1$ are values reported in literature^{14,26}.

V. CONCLUSION

In this work, we have outlined a new strategy for engineering multiplet-driven photomagnetism in collinear AFMs. We demonstrate that substituting TM ions in isostructural compounds is effective for tuning the AFM ground state and enhancing photomagnetic response. In the TM-thiophosphates, we show that even introducing 10% of Ni ions into MnPS_3 – a material characterized by minimal orbital angular momentum and inherently weak anisotropy – dramatically enhances photomagnetism while leaving the ground state relatively untouched. Further tuning the chemical composition, we demonstrate precise control over the AFM ground state exchange and anisotropy, as well as the symmetry of the magnon mode. Control over these static and dynamic properties is essential from a device engineering perspective. While we sampled the full range of mixed compositions in this study, the TM-ion substitution fraction can be even more finely tuned to achieve desired parameters and performance.

Understanding the microscopic mechanisms behind ultrafast photomagnetic processes remains a fundamental challenge⁵⁸. In light of this, mixing the compounds allows for a direct comparison of the photomagnetic response of Mn and Ni multiplet resonances within the same sample, which allows us to distill important considerations for the mechanisms of magnon generation. Our *ab-initio* calculations demonstrate how spin conservation, orbital angular momentum and the degree of localization of multiplet resonances affect the magnitude of excited magnons. The $^3A_{1g}$ resonance in Ni^{2+} , in particular, drives the largest magnon response across the entire spectrum of mixed compounds due to its localized nature and the large unquenched orbital angular momentum of the excited state. The $^3T_{1g}$ multiplet, on the other hand, is delocalized across the ligands and may not be properly considered a *d-d* excitation. Our observations also highlight the advantages of working with a low-symmetry system, in which multiplet resonances are non-degenerate. For comparison, in a high symmetry system such as NiO , the perfect cubic crystal field ensures that there are no *d-d* excitonic transitions between 1 and 1.6 eV⁵⁹.

These results naturally point to the broader exploration of TM dopants. In the TM-thiophosphate family, Co and Fe are compelling candidates, with the former hosting a partially filled t_{2g} manifold and significant unquenched orbital angular momentum in the ground state compared to Ni and Mn, and the latter having the largest single-ion anisotropy of the family⁶⁰. Altogether, the mixed TM-thiophosphates constitute a rich platform for the exploration and engineering of antiferromagnetic ground states and photomagnetic effects^{61,62}. Beyond this family of materials, the principles we outline in this work can be applied to any collinear AFM where TM ions may be chemically substituted with ions of varying *d*-orbital occupation. As demonstrated here, intentional targeting of the multiplet resonances of dopants can significantly increase the efficacy and flexibility of photomagnetism in these materials.

MATERIALS AND METHODS

A. Sample growing and characterization

Chemical vapor transport (CVT) technique is employed to grow bulk single crystals of $(\text{Mn}_x\text{Ni}_{1-x})\text{PS}_3$ series of compounds following the synthesis method reported by Susner et al. with slight modification⁴¹. Halogens (I_2 or Br_2) were employed as the transport agent in the synthetic process. Stoichiometric amounts of manganese (Mn) powder, nickel (Ni) powder, phosphorus (P) lump and sulfur (S) were sealed in an evacuated quartz tube (ampoule) with an inner pressure in the range of 10^{-5} to 10^{-6} Torr. In addition to the elemental constituents (Mn, Ni, P and S), a small amount (2 mg/cc) of iodine spheres were added inside the ampoule to act as the transport agent. The sealed ampoules were then subjected to a two-zone horizontal tube furnace.

Initially, the source zone was kept at 650°C and the growth zone at 750°C for 48 hours. This arrangement was made to allow the constituents to react completely and prevent the back transport or formation of undesired additional phases. After that, the temperature of the source zone gradually increased to 750°C and that of the growth zone was lowered to 700°C . This arrangement lasted for another 120 hours. Finally, the temperatures of both the zones were lowered down, and the plate-like crystals were subsequently obtained from the ampoule for further characterizations and experiments.

The characterization of the samples (composition, homogeneity) was performed by energy-dispersive X-ray spectroscopy (EDS). The EDS measurements were carried out on an Ultra-high Resolution Scanning Electron Microscope (SEM) SU8020 (Hitachi) equipped with a X-MaxN (Oxford) Silicon Drift Detector (SDD). Selected single crystals were glued to a carbon tape and analyzed by semiquantitative EDS at a 20 kV acceleration voltage. The details are presented in Supplementary Sec. 1.

B. Magnetometry characterization

The magnetometry measurements were performed using the Vibrating Sample Magnetometer (VSM) of a Physical Property Measurement System (PPMS) of Quantum Design. The pick-up coil was placed in the (vertical) constant magnetic field produced by the superconducting solenoid; one measures only the component of the magnetization M along the field H direction. For measuring parallel and perpendicular field configurations, the sample was taken out of the holder and remounted.

C. Magneto-optical measurements

Data shown in Fig. 1b, Fig. 4 of the main text are performed with a Spectra Physics Spitfire Ace system, operating at a repetition rate 1 kHz. The Spitfire Ace amplifies femtosecond pulses from a mode-locked MaiTai Ti:Sapphire seed laser (photon energy of 1.55 eV, pulse duration of 130 fs). A part of the generated beam is sent to a TOPAS-Prime collinear OPA, which generates pulses with tunable wavelengths from 0.06 - 6.56 eV, and is used as a pump. The remaining power, separated by the beamsplitter, is used as a probe. The pump is chopped at 500 Hz and focused to a spot size of $\approx 200 \mu\text{m}$; the probe pulse is focused to a spot size of $\approx 120 \mu\text{m}$.

The mixed compounds measured here were exfoliated to produce a smooth surface. The samples are bulk-like, with an estimated thickness between $100 \mu\text{m}$ to 1 mm.

Data shown in Fig. 1c of the main text (optical absorbance) are performed by using a halogen light source (Ocean Optics HL-2000) with a spectrum from 400 nm to 1600 nm. Thin NiPS_3 (MnPS_3) flakes of thickness $\approx 10 \mu\text{m}$ and size $\approx 200 \mu\text{m}$ are prepared and put onto a CaF_2 substrate. The light is focused to a spot size of $< 10 \mu\text{m}$ on the sample by an objective, and the transmitted light is collected by another objective, and focused onto a grating spectrometer, where an infrared (visible) camera is used to detect the transmitted intensity.

Data shown in Fig. 2 of the main text are performed with the PHAROS BURST laser system, which is an oscillator operating at 76 MHz, with a Yb:KGW crystal acting as an active medium. A regenerative amplifier (RA) and pulse-picker then allows the user to change the repetition rate without affecting the internal operation. We operate the PHAROS BURST RA at 75 KHz with 267 μJ of pulse energy, which is further pulse-picked down to 5 kHz for experiments to avoid excessive average-power heating of the sample. The probe pulses have a pulse duration of 170 fs with a photon energy of 1.2 eV. A percentage of the power of PHAROS pulses are split and used to see the ORPHEUS-HP optical parametric amplifier

(OPA), which generates tunable pump wavelengths from 0.8 - 3 eV with a bandwidth of 20-30 meV, depending on the pump photon energy. The pump is chopped at 2.5 kHz, and focused to a spot size of $(94 \pm 15 \times 78 \pm 11)$ μm full-width-at-half-maximum (FWHM) on the sample surface. The remaining power is used for the probe. To maximize the second harmonic generation signal, the probe pulses are focused tightly to a spot size of ≈ 50 μm .

The mixed compounds measured here were exfoliated to produce a smooth surface. The samples are bulk-like, with an estimated thickness ~ 100 μm .

ACKNOWLEDGMENTS

The authors thank B. A. Ivanov for fruitful discussions, and K. Saeedi Ilkhchy and C. Berkhout for their technical support. We are grateful to Prof. Hari Shrikant for insightful discussions. This work is supported by ERC grant 101078206 ASTRAL; programme “Materials for the Quantum Age” (QuMat, registration number 024.005.006), which is part of the Gravitation programme financed by the Dutch Ministry of Education, Culture and Science (OCW); the European Union Horizon 2020 and innovation program under the European Research Council ERC grant agreement no. 856538 (3D-MAGiC), and the European Research Council ERC grant agreement no. 101054664 273 (SPARTACUS). M. Na acknowledges the support of the Natural Sciences and Engineering Research Council of Canada (NSERC) PDF fellowship.

This work was authored in part by the National Laboratory of the Rockies for the U.S. Department of Energy (DOE) under Contract No. DE-AC36-08GO28308. Funding was provided by the Computational Chemical Sciences program within the Office of Basic Energy Sciences, U.S. Department of Energy. S.A. acknowledges the use of the National Energy Research Scientific Computing Center, under Contract No. DE-AC02-05CH11231 using NERSC award BES-ERCAP0021783 and S.A. also acknowledges that a portion of the research was performed using computational resources sponsored by the Department of Energy’s Office of Energy Efficiency and Renewable Energy and located at the National Laboratory of the Rockies. The views expressed in the article do not necessarily represent the views of the DOE or the U.S. Government. The U.S. Government retains and the publisher, by accepting the article for publication, acknowledges that the U.S. Government retains a nonexclusive, paid-up, irrevocable, worldwide license to publish or reproduce the published form of this work, or allow others to do so, for U.S. Government purposes.

CONTRIBUTIONS

D.A., A.C., and M.N conceived the project. D.A., Th.R. and A.V.K. supervised the study. V.R., M.N. and D.A. performed the static and pump-probe experiments. D.P., M.V.S. and S.A. provided the theoretical model. A.C. provided the samples. E.K. and A.I provided the EDS characterization, A.V. provided the magnetometry. K.M., V.R., M.N., and P.C. performed optical absorption experiments. D.K., P.K., contributed to discussion and treatment of the experimental results. M.N., V.R., S.A., and D.A. wrote original draft with feedback from all the co-authors.

COMPETING INTERESTS

The authors declare no competing interests.

DATA AVAILABILITY

All data supporting the findings of this paper are available from the corresponding authors upon request.

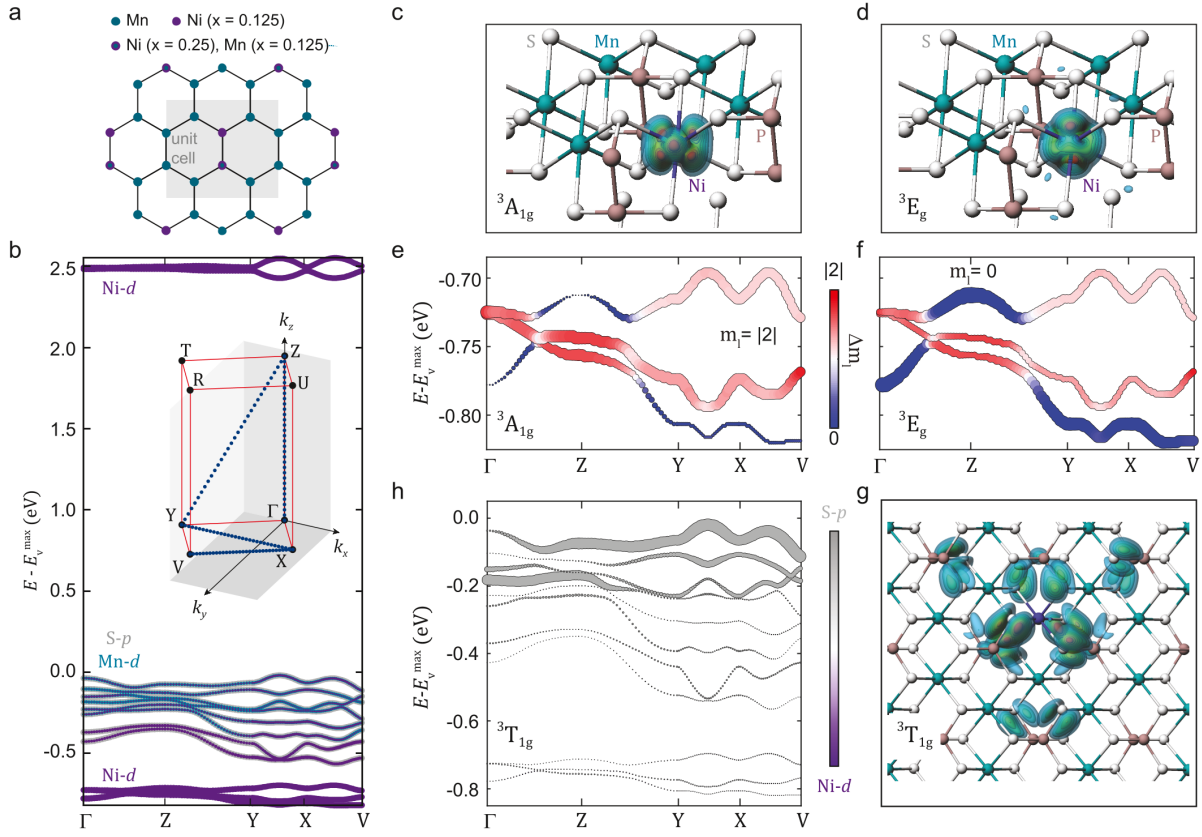
REFERENCES

- ¹U Enz, W Lems, R Metselaar, P Rijniere, and R Teale. Photomagnetic effects. *IEEE Transactions on Magnetics*, 5(3): 467–472, 1969. doi:10.1109/TMAG.1969.1066522.
- ²Tobias Kampfrath, Koichiro Tanaka, and Keith A Nelson. Resonant and nonresonant control over matter and light by intense terahertz transients. *Nature Photonics*, 7(9):680–690, 2013.
- ³N Tesařová, P Němec, E Rozkotová, J Zemen, T Janda, D Butkovičová, F Trojánek, K Olejník, V Novák, P Malý, et al. Experimental observation of the optical spin-orbit torque. *Nature Photonics*, 7(6):492–498, 2013.
- ⁴Takuya Satoh, Yuki Terui, Rai Moriya, Boris A Ivanov, Kazuya Ando, Eiji Saitoh, Tsutomu Shimura, and Kazuo Kuroda. Directional control of spin-wave emission by spatially shaped light. *Nature Photonics*, 6(10):662–666, 2012.
- ⁵Anne Bleuzen, Valérie Marvaud, Corine Mathoniere, Barbara Sieklucka, and Michel Verdaguer. Photomagnetism in clusters and extended molecule-based magnets. *Inorganic chemistry*, 48(8):3453–3466, 2009.
- ⁶Jakub J Zakrzewski, Michal Liberka, Junhao Wang, Szymon Chorazy, and Shin-ichi Ohkoshi. Optical phenomena in molecule-based magnetic materials. *Chemical Reviews*, 124(9):5930–6050, 2024.
- ⁷A. Stupakiewicz, K. Szerenos, D. Afanasiev, A. Kirilyuk, and A. V. Kimel. Ultrafast nonthermal photo-magnetic recording in a transparent medium. *Nature*, 542(7639):71–74, 2017. ISSN 1476-4687. doi:10.1038/nature20807.
- ⁸S. Baierl, M. Hohenleutner, T. Kampfrath, A. K. Zvezdin, A. V. Kimel, R. Huber, and R. V. Mikhaylovskiy. Nonlinear spin control by terahertz-driven anisotropy fields. *Nature Photonics*, 10(11):715–718, 2016. ISSN 1749-4893. doi: 10.1038/nphoton.2016.181.
- ⁹AS Disa, J Curtis, M Fechner, A Liu, A Von Hoegen, M Först, TF Nova, P Narang, A Maljuk, AV Boris, et al. Photo-induced high-temperature ferromagnetism in ytio3. *Nature*, 617(7959):73–78, 2023.
- ¹⁰AV Kimel, A Kirilyuk, PA Usachev, RV Pisarev, AM Balbashov, and Th Rasing. Ultrafast non-thermal control of magnetization by instantaneous photomagnetic pulses. *Nature*, 435(7042):655–657, 2005.
- ¹¹AM Kalashnikova, AV Kimel, RV Pisarev, VN Gridnev, Andrei Kirilyuk, and Th Rasing. Impulsive generation of coherent magnons by linearly polarized light? format?; in the easy-plane antiferromagnet febo 3. *Physical review letters*, 99(16): 167205, 2007.
- ¹²Andrei Kirilyuk, Alexey V. Kimel, and Theo Rasing. Ultrafast optical manipulation of magnetic order. *Reviews of Modern Physics*, 82(3):2731–2784, 2010. doi:10.1103/RevModPhys.82.2731.
- ¹³Dmytro Afanasiev, JR Hortensius, BA Ivanov, Alireza Sasani, Eric Bousquet, Yaroslav M Blanter, Rostislav V Mikhaylovskiy, Alexey V Kimel, and AD Caviglia. Ultrafast control of magnetic interactions via light-driven phonons. *Nature materials*, 20(5):607–611, 2021.
- ¹⁴Dmytro Afanasiev, Jorrit R. Hortensius, Mattias Matthiesen, Samuel Mañas-Valero, Makars Šiškins, Martin Lee, Edouard Lesne, Herre S. J. van der Zant, Peter G. Steeneken, Boris A. Ivanov, Eugenio Coronado, and Andrea D. Caviglia. Controlling the anisotropy of a van der Waals antiferromagnet with light. *Science Advances*, 7(23):eabf3096, 2021. doi:10.1126/sciadv.abf3096.
- ¹⁵R. V. Mikhaylovskiy, T. J. Huisman, V. A. Gavrichkov, S. I. Polukeev, S. G. Ovchinnikov, D. Afanasiev, R. V. Pisarev, Th. Rasing, and A. V. Kimel. Resonant pumping of d-d crystal field electronic transitions as a mechanism of ultrafast optical control of the exchange interactions in iron oxides. *Physical Review Letters*, 125(15):157201, 2020. doi:10.1103/PhysRevLett.125.157201.
- ¹⁶A Ron, S Chaudhary, G Zhang, H Ning, E Zoghlin, SD Wilson, RD Averitt, G Refael, and D Hsieh. Ultrafast enhancement of ferromagnetic spin exchange induced by ligand-to-metal charge transfer. *Physical Review Letters*, 125(19):197203, 2020.
- ¹⁷Tobia F Nova, Andrea Cartella, Alice Cantaluppi, Michael Först, Davide Bossini, Rostislav V Mikhaylovskiy, Aleksei V Kimel, Roberto Merlin, and Andrea Cavalleri. An effective magnetic field from optically driven phonons. *Nature Physics*, 13(2):132–136, 2017.
- ¹⁸P. Němec, M. Fiebig, T. Kampfrath, and A. V. Kimel. Antiferromagnetic opto-spintronics. *Nature Physics*, 14(3): 229–241, 2018. ISSN 1745-2481. doi:10.1038/s41567-018-0051-x.
- ¹⁹Takuya Satoh, Ryugo Iida, Takuya Higuchi, Manfred Fiebig, and Tsutomu Shimura. Writing and reading of an arbitrary optical polarization state in an antiferromagnet. *Nature Photonics*, 9(1):25–29, 2015.
- ²⁰Tobias Kampfrath, Alexander Sell, Gregor Klatt, Alexej Pashkin, Sebastian Mährlein, Thomas Dekorsy, Martin Wolf, Manfred Fiebig, Alfred Leitenstorfer, and Rupert Huber. Coherent terahertz control of antiferromagnetic spin waves. *Nature Photonics*, 5(1):31–34, 2011.
- ²¹S. Schlauderer, C. Lange, S. Baierl, T. Ebnert, C. P. Schmid, D. C. Valovcin, A. K. Zvezdin, A. V. Kimel, R. V. Mikhaylovskiy, and R. Huber. Temporal and spectral fingerprints of ultrafast all-coherent spin switching. *Nature*, 569 (7756):383–387, 2019. ISSN 1476-4687. doi:10.1038/s41586-019-1174-7.
- ²²A. Stupakiewicz, K. Szerenos, M. D. Davydova, K. A. Zvezdin, A. K. Zvezdin, A. Kirilyuk, and A. V. Kimel. Selection rules for all-optical magnetic recording in iron garnet. *Nature Communications*, 10(1):612, 2019. ISSN 2041-1723. doi:10.1038/s41467-019-08458-w.
- ²³Alexandre Marciniak, Stefano Marcantoni, Francesca Giusti, Filippo Glerean, Giorgia Sparapassi, Tobia Nova, Andrea Cartella, Simone Latini, Francesco Valiera, Angel Rubio, et al. Vibrational coherent control of localized d–d electronic excitation. *Nature Physics*, 17(3):368–373, 2021.
- ²⁴Lawrence L Lohr Jr. Spin-forbidden electronic excitations in transition metal complexes. *Coordination Chemistry Reviews*, 8(3):241–259, 1972.
- ²⁵Gabriel Fitzky, Makoto Nakajima, Yohei Koike, Alfred Leitenstorfer, and Takayuki Kurihara. Ultrafast control of magnetic anisotropy by resonant excitation of 4 f electrons and phonons in sm 0.7 er 0.3 feo 3. *Physical Review Letters*, 127(10):107401, 2021.
- ²⁶Mattias Matthiesen, Jorrit R. Hortensius, Samuel Mañas-Valero, Itzik Kapon, Dumitru Dumcenco, Enrico Giannini, Makars Šiškins, Boris A. Ivanov, Herre S. J. van der Zant, Eugenio Coronado, Alexey B. Kuzmenko, Dmytro Afanasiev, and Andrea D. Caviglia. Controlling magnetism with light in a zero orbital angular momentum antiferromagnet. *Physical Review Letters*, 130(7):076702, 2023. doi:10.1103/PhysRevLett.130.076702.
- ²⁷Ryugo Iida, Takuya Satoh, Tsutomu Shimura, Kazuo Kuroda, BA Ivanov, Yusuke Tokunaga, and Yoshinori Tokura. Spectral dependence of photoinduced spin precession in dyfeo 3. *Physical Review B—Condensed Matter and Materials Physics*, 84(6):064402, 2011.

- ²⁸Carina A. Belvin, Edoardo Baldini, Ilkem Ozge Ozel, Dan Mao, Hoi Chun Po, Clifford J. Allington, Suhan Son, Beom Hyun Kim, Jonghyeon Kim, Inho Hwang, Jae Hoon Kim, Je-Geun Park, T. Senthil, and Nuh Gedik. Exciton-driven antiferromagnetic metal in a correlated van der Waals insulator. *Nature Communications*, 12(1):4837, 2021. ISSN 2041-1723. doi:10.1038/s41467-021-25164-8.
- ²⁹Fabian Mertens, David Mönkebüscher, Umut Parlak, Carla Boix-Constant, Samuel Mañas-Valero, Margherita Matzer, Rajdeep Adhikari, Alberta Bonanni, Eugenio Coronado, Alexandra M Kalashnikova, et al. Ultrafast coherent thz lattice dynamics coupled to spins in the van der waals antiferromagnet feps3. *Advanced Materials*, 35(6):2208355, 2023.
- ³⁰Bheema Lingam Chittari, Youngju Park, Dongkyu Lee, Moonup Han, Allan H. MacDonald, Euyheon Hwang, and Jeil Jung. Electronic and magnetic properties of single-layer MPX₃ metal phosphorous trichalcogenides. *Physical Review B*, 94(18):184428, 2016. doi:10.1103/PhysRevB.94.184428.
- ³¹Rabindra Basnet and Jin Hu. Understanding and tuning magnetism in van der Waals-type metal thiophosphates. *Nanoscale*, 2024. doi:10.1039/D4NR01577K.
- ³²Jun-Yi Shan, M Ye, H Chu, Sungmin Lee, Je-Geun Park, L Balents, and D Hsieh. Giant modulation of optical nonlinearity by floquet engineering. *Nature*, 600(7888):235–239, 2021.
- ³³Je-Ho Lee, Seungyeol Lee, Youngsu Choi, Lukas Gries, Rüdiger Klingeler, Kalaivanan Raju, Rajesh Kumar Ulaganathan, Raman Sankar, Maeng-Je Seong, and Kwang-Yong Choi. Optical Probe of Magnetic Ordering Structure and Spin-Entangled Excitons in Mn-Substituted NiPS₃. *Advanced Functional Materials*, 34(39):2405153, 2024. ISSN 1616-3028. doi:10.1002/adfm.202405153.
- ³⁴Shingo Toyoda, Jonathon Kruppe, Kohtaro Yamakawa, James Analytis, and Joseph Orenstein. Phase control of spin waves in the van der Waals antiferromagnet NiPS_3 . *Physical Review B*, 109(6):064408, 2024. doi:10.1103/PhysRevB.109.064408.
- ³⁵Florian Dirnberger, Rezlind Bushati, Biswajit Datta, Ajesh Kumar, Allan H MacDonald, Edoardo Baldini, and Vinod M Menon. Spin-correlated exciton–polaritons in a van der waals magnet. *Nature Nanotechnology*, 17(10):1060–1064, 2022.
- ³⁶Dmitry Lebedev, J Tyler Gish, Ethan S Garvey, S Carin Gavin, Thomas W Song, Manuel R Tiscareno, Kenji Watanabe, Takashi Taniguchi, Jan Konecny, Zdeněk Sofer, et al. Ultranarrow electroluminescence from magnetic excitons in the van der waals antiferromagnetic semiconductor nips3. *Nature Communications*, 16(1):10550, 2025.
- ³⁷Soonmin Kang, Kangwon Kim, Beom Hyun Kim, Jonghyeon Kim, Kyung Ik Sim, Jae-Ung Lee, Sungmin Lee, Kisoo Park, Seokhwan Yun, Taehun Kim, Abhishek Nag, Andrew Walters, Mirian Garcia-Fernandez, Jiemin Li, Laurent Chapon, Ke-Jin Zhou, Young-Woo Son, Jae Hoon Kim, Hyeonsik Cheong, and Je-Geun Park. Coherent many-body exciton in van der Waals antiferromagnet NiPS₃. *Nature*, 583(7818):785–789, 2020. ISSN 1476-4687. doi:10.1038/s41586-020-2520-5.
- ³⁸Brian Cunningham, Myrta Grüning, Dimitar Pashov, and Mark van Schilfgaarde. QSGW: Quasiparticle Self Consistent GW with Ladder Diagrams in W. *Physical Review B*, 108:165104, 2023. URL <https://journals.aps.org/prb/abstract/10.1103/PhysRevB.108.165104>.
- ³⁹Dimitar Pashov, Swagata Acharya, Walter R. L. Lambrecht, Jerome Jackson, Kirill D. Belashchenko, Athanasios Chantisi, Francois Jamet, and Mark van Schilfgaarde. Questaal: a package of electronic structure methods based on the linear muffin-tin orbital technique. *Comp. Phys. Comm.*, 249:107065, 2020. URL <https://www.sciencedirect.com/science/article/pii/S0010465519303868?via%3Dihub>.
- ⁴⁰Swagata Acharya, Dimitar Pashov, Cedric Weber, Mark van Schilfgaarde, Alexander I. Lichtenstein, and Mikhail I. Katsnelson. A theory for colors of strongly correlated electronic systems. *Nature Communications*, 14(1):5565, September 2023. ISSN 2041-1723. doi:10.1038/s41467-023-41314-6. URL <https://doi.org/10.1038/s41467-023-41314-6>.
- ⁴¹Michael A. Susner, Marius Chyasnovichyus, Michael A. McGuire, Panchapakesan Ganesh, and Petro Maksymovych. Metal thio- and selenophosphates as multifunctional van der waals layered materials. *Advanced Materials*, 29(38):1602852, 2017. doi:<https://doi.org/10.1002/adma.201602852>. URL <https://advanced.onlinelibrary.wiley.com/doi/abs/10.1002/adma.201602852>.
- ⁴²P. A. Joy and S. Vasudevan. Magnetism in the layered transition-metal thiophosphates MPS₃ (M=Mn, Fe, and Ni). *Physical Review B*, 46(9):5425–5433, 1992. doi:10.1103/PhysRevB.46.5425.
- ⁴³Rabindra Basnet, Aaron Wegner, Krishna Pandey, Stephen Stormont, and Jin Hu. Highly sensitive spin-flop transition in antiferromagnetic van der Waals material MPS₃ (M = Ni and Mn). *Physical Review Materials*, 5(6):064413, 2021. ISSN 2475-9953. doi:10.1103/PhysRevMaterials.5.064413.
- ⁴⁴Hao Chu, Chang Jae Roh, Joshua O. Island, Chen Li, Sungmin Lee, Jingjing Chen, Je-Geun Park, Andrea F. Young, Jong Seok Lee, and David Hsieh. Linear magnetoelectric phase in ultrathin MnPS₃ probed by optical second harmonic generation. *Physical Review Letters*, 124(2):027601, 2020. doi:10.1103/PhysRevLett.124.027601.
- ⁴⁵Qi Zhang, Kyle Hwangbo, Chong Wang, Qianni Jiang, Jiun-Haw Chu, Haidan Wen, Di Xiao, and Xiaodong Xu. Observation of giant optical linear dichroism in a zigzag antiferromagnet FePS₃. *Nano Letters*, 21(16):6938–6945, 2021. ISSN 1530-6984. doi:10.1021/acs.nanolett.1c02188.
- ⁴⁶D. Khusyainov, T. Gareev, V. Radovskaia, K. Sampathkumar, S. Acharya, M. Šiškins, S. Mañas-Valero, B. A. Ivanov, E. Coronado, Th. Rasing, A. V. Kimel, and D. Afanasiev. Ultrafast laser-induced spin–lattice dynamics in the van der Waals antiferromagnet CoPS₃. *APL Materials*, 11(7):071104, 2023. ISSN 2166-532X. doi:10.1063/5.0146128.
- ⁴⁷Miłosz Rybak, Paulo E. Faria Junior, Tomasz Woźniak, Pawel Scharoch, Jaroslav Fabian, and Magdalena Birowska. Magneto-optical anisotropies of two-dimensional antiferromagnetic M P X₃ from first principles. *Physical Review B*, 109(5):054426, 2024. ISSN 2469-9950, 2469-9969. doi:10.1103/PhysRevB.109.054426.
- ⁴⁸Kiichi Okuda, Ko Kurosawa, Shozo Saito, Makoto Honda, Zhihong Yu, and Muneyuki Date. Magnetic properties of layered compound mnps3. *Journal of the Physical Society of Japan*, 55(12):4456–4463, 1986.
- ⁴⁹A. R. Wildes, H. M. Rønnow, B. Roessli, M. J. Harris, and K. W. Godfrey. Static and dynamic critical properties of the quasi-two-dimensional antiferromagnet MnPS_3 . *Physical Review B*, 74(9):094422, 2006. doi:10.1103/PhysRevB.74.094422.
- ⁵⁰D Lançon, R. A Ewings, T Guidi, F Formisano, and AR Wildes. Magnetic exchange parameters and anisotropy of the quasi-two-dimensional antiferromagnet nips 3. *Physical Review B*, 98(13):134414, 2018.
- ⁵¹Ziye Lu, Xinyu Yang, Lin Huang, Xiyu Chen, Meifeng Liu, Jin Peng, Shuai Dong, and Jun-Ming Liu. Evolution of magnetic phase in two-dimensional van der Waals Mn_{1-x}Ni_xPS₃ single crystals. *Journal of Physics: Condensed Matter*, 34(35):354005, 2022. ISSN 0953-8984. doi:10.1088/1361-648X/ac7a80.
- ⁵²Clifford J Allington, Carina A Belvin, Urban FP Seifert, Mengxing Ye, Tommy Tai, Edoardo Baldini, Suhan Son, Junghyun Kim, Jaena Park, Je-Geun Park, et al. Distinct optical excitation mechanisms of a coherent magnon in a van

- der waals antiferromagnet. *Physical Review Letters*, 134(6):066903, 2025.
- ⁵³A. R. Wildes, B. Roessli, B. Lebech, and K. W. Godfrey. Spin waves and the critical behaviour of the magnetization in MnPS₃. *Journal of Physics: Condensed Matter*, 10(28):6417, 1998. ISSN 0953-8984. doi:10.1088/0953-8984/10/28/020.
- ⁵⁴Dipankar Jana, Swagata Acharya, Milan Orlita, Clement Augeras, Dimitar Pashov, Mark Van Schilfgaarde, Marek Potemski, and Maciej Koperski. Deconstruction of the anisotropic magnetic interactions from spin-entangled optical excitations in van der waals antiferromagnets. *Advanced Science*, page e05834, 2025.
- ⁵⁵E. J. K. B. Banda. Optical absorption of NiPS₃ in the near-infrared, visible and near-ultraviolet regions. *Journal of Physics C: Solid State Physics*, 19(36):7329, 1986. ISSN 0022-3719. doi:10.1088/0022-3719/19/36/023.
- ⁵⁶Jonghyeon Kim, Junghyun Kim, Beom Hyun Kim, Je-Geun Park, and Jae Hoon Kim. Anisotropic optical band structure of van der Waals antiferromagnet NiPS₃. *Physical Review B*, 110(18):L180406, 2024. ISSN 2469-9950, 2469-9969. doi: 10.1103/PhysRevB.110.L180406.
- ⁵⁷Maciej Śmiertka, Michał Rygała, Katarzyna Posmyk, Paulina Peksa, Mateusz Dyksik, Dimitar Pashov, Kseniia Mosina, Zdeněk Sofer, Mark van Schilfgaarde, Florian Dirnberger, et al. Distinct magneto-optical response of frenkel and wannier excitons in crsbr. *Nature Communications*, 2026. doi:https://doi.org/10.1038/s41467-026-68482-5.
- ⁵⁸Thomas J. Penfold, J. Olof Johansson, and Julien Eng. Towards understanding and controlling ultrafast dynamics in molecular photomagnets. *Coordination Chemistry Reviews*, 494:215346, 2023. ISSN 0010-8545. doi: 10.1016/j.ccr.2023.215346.
- ⁵⁹V Propach and D Reinen. Über die farbe von "nio"/the different colours of "nio". *Zeitschrift für Naturforschung B*, 33(6):619–621, 1978.
- ⁶⁰Jae-Ung Lee, Sungmin Lee, Ji Hoon Ryoo, Soonmin Kang, Tae Yun Kim, Pilkwang Kim, Cheol-Hwan Park, Je-Geun Park, and Hyeonsik Cheong. Ising-type magnetic ordering in atomically thin FePS₃. *Nano Letters*, 16(12):7433–7438, 2016. ISSN 1530-6984. doi:10.1021/acs.nanolett.6b03052.
- ⁶¹Jiayu Li, Qiushi Yao, Lin Wu, Zongxiang Hu, Boya Gao, Xiangang Wan, and Qihang Liu. Designing light-element materials with large effective spin-orbit coupling. *Nature Communications*, 13:919, 2022. ISSN 2041-1723. doi:10.1038/s41467-022-28534-y. URL <https://www.ncbi.nlm.nih.gov/pmc/articles/PMC8854432/>.
- ⁶²Songsong Yan, Yongping Du, Xiaouo Zhang, Xiangang Wan, and Di Wang. First-principles study of magnetic interactions and excitations in antiferromagnetic van der waals material mpx₃ (m= mn, fe, co, ni; x= s, se). *Journal of Physics: Condensed Matter*, 36(6):065502, 2023.

EXTENDED DATA



Extended Data Fig. 1. Ab-initio calculation of Ni²⁺ multiplets. Excitonic wavefunctions are computed in the framework of QSGW³⁸ theory for the mixed compounds Mn_{1-x}Ni_xPS₃, with $x = 0.25$ (details in Supplementary Sec. 6). (a) The in-plane distribution of Mn and Ni ions for the $x = 0.125$ and $x = 0.25$ alloys. (b) The electronic band structure of Mn_{1-x}Ni_xPS₃, for $x = 0.25$. The colors of the markers indicate the weight of S-*p*, Mn-*d*, Ni-*d* orbitals, respectively. The Brillouin zone and high-symmetry points are shown in the inset, with the *k*-path denoted in blue. (c,d,g) The wavefunction of the excitonic-hole for the ³A_{1g}, ³E_g and ³T_{1g} excitations. The Ni and Mn ions are shown in purple and turquoise, respectively. S and P are shown in gray and brown. The ³A_{1g} and ³E_g excitations are localized to the Ni-ion, while the ³T_{1g} state is delocalized over multiple hexagonal plaquette. (e,f,h) Electronic band structure plotted along *k*-path in the inset of b for the ³A_{1g}, ³E_g and ³T_{1g} excitations. Marker size indicates the weight of the excitonic hole $c_{n,\mathbf{k}}$, raised to the power of 4 for visualization purposes. Projection show that the ³A_{1g} (³E_g) excitation is projected onto the $m_l = |2|$ (0) Ni-*d* states, while the ³T_{1g} excitation is delocalized over the S-*p* valence bands.